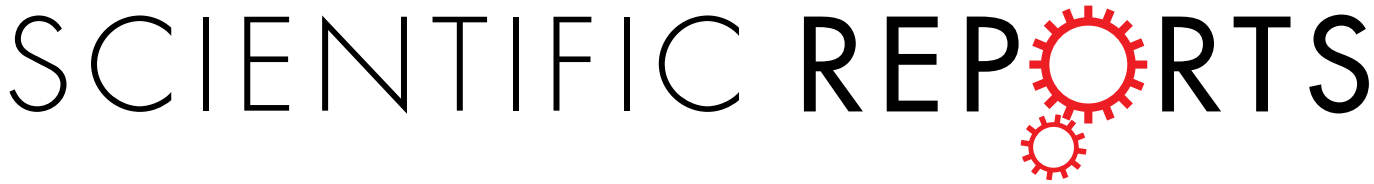

OPEN

Photoresponsivity of an all-semimetal heterostructure based on graphene and WTe_2

Received: 2 May 2018
Accepted: 28 June 2018
Published online: 27 August 2018

Yujie Liu[1,3], Chuan Liu[1,3], Xiaomu Wang[1,3], Liang He[1,3], Xiangang Wan[2,3], Yongbing Xu[1,3], Yi Shi[1,3], Rong Zhang[1,3] & Fengqiu Wang[1,3]

Heterostructures based on two-dimensional (2D) materials have sparked wide interests in both fundamental physics and applied devices. Recently, Dirac/Weyl semimetals are emerging as capable functional materials for optoelectronic devices. However, thus far the interfacial coupling of an all-semimetal 2D heterostructure has not been investigated, and its effects on optoelectronic properties remain less well understood. Here, a heterostructure comprising of all semi-metallic constituents, namely graphene and WTe_2, is fabricated. Standard photocurrent measurements on a graphene/WTe_2 phototransistor reveal a pronounced photocurrent enhancement (a photoresponsivity ~8.7 A/W under 650 nm laser illumination). Transport and photocurrent mapping suggest that both photovoltaic and photothermoelectric effects contribute to the enhanced photoresponse of the hybrid system. Our results help to enrich the understanding of new and emerging device concepts based on 2D layered materials.

Heterostructures based on van der Waals (vdWs)-bonded layered materials have opened new avenues for fundamental scientific studies and applied devices[1–4]. The absence of dangling bonds on the surfaces of vdWs materials enables the creation of high-quality hetero-interfaces without the constraints of lattice matching and processing compatibility[5,6]. Indeed, vdWs heterostructures have been realized using different combinations of 2D materials, including metallic graphene[7], insulating boron nitride (BN)[8] and semiconducting transition metal dichalcogenides (TMDCs)[9,10]. While interesting electronic and optical properties of these 2D materials are being investigated, peculiar physics at the hetero-interfaces are attracting ever growing attentions[11–14]. Elucidating the interfacial effects and coupling mechanisms for different types of heterostructures and constituents compounds will provide important guidelines for developing functional 2D materials heterostructures.

In addition to conventional semiconductor and metal materials, Dirac/Weyl semimetals are emerging as capable functional quantum materials for optoelectronic and photonic applications[15–21]. Graphene is, strictly speaking, an exemplary 2D Dirac semimetal. Owing to its unique physical properties, *e.g.* mono-atomic thickness, universal optical absorption and gate tunable Fermi level, a variety of remarkable optoelectronic devices have been demonstrated by forming different types of graphene heterostructures. For instance, stacking graphene with semiconductors can form a versatile Schottky-type metal-semiconductor junction that is widely used in photodetection, solar energy collection and Schottky diode, *etc*[22–26]. Graphene-hexagonal boron nitride (hBN) heterostructure, as a paradigm of semimetal-insulator junction, offers a huge potential application in the fabrication of atomically thin field-effect transistors, resonant tunneling transistors and diodes[27–29]. In addition, due to the work function difference, graphene is usually doped by 3D metal contact, which can effectively improve the performance of graphene-based photodetectors[30–34]. Although considerable amount of work has focused on graphene heterostructures, graphene-semimetal heterostructures (as well as the other vdWs heterostructures comprised of purely semimetallic constituents) have remained less well studied[35–37].

In this work, the optoelectronic properties of a hetero-interface formed by semimetal graphene and WTe_2 is investigated. WTe_2 is chosen to form an all-semimetal 2D heterostructure as it belongs to an emerging class of Weyl semimetal with significant relevance to optics and photonics[38–42]. In addition to providing potentially better metallic contact than commonly used 3D metals[43], study of the fundamental properties of such heterostructures

[1]School of Electronic Science and Engineering, Nanjing University, Nanjing, 210093, China. [2]School of Physics, Nanjing University, Nanjing, 210093, China. [3]Collaborative Innovation Center of Advanced Microstructures, Nanjing University, Nanjing, 210093, China. Correspondence and requests for materials should be addressed to F.W. (email: fwang@nju.edu.cn)

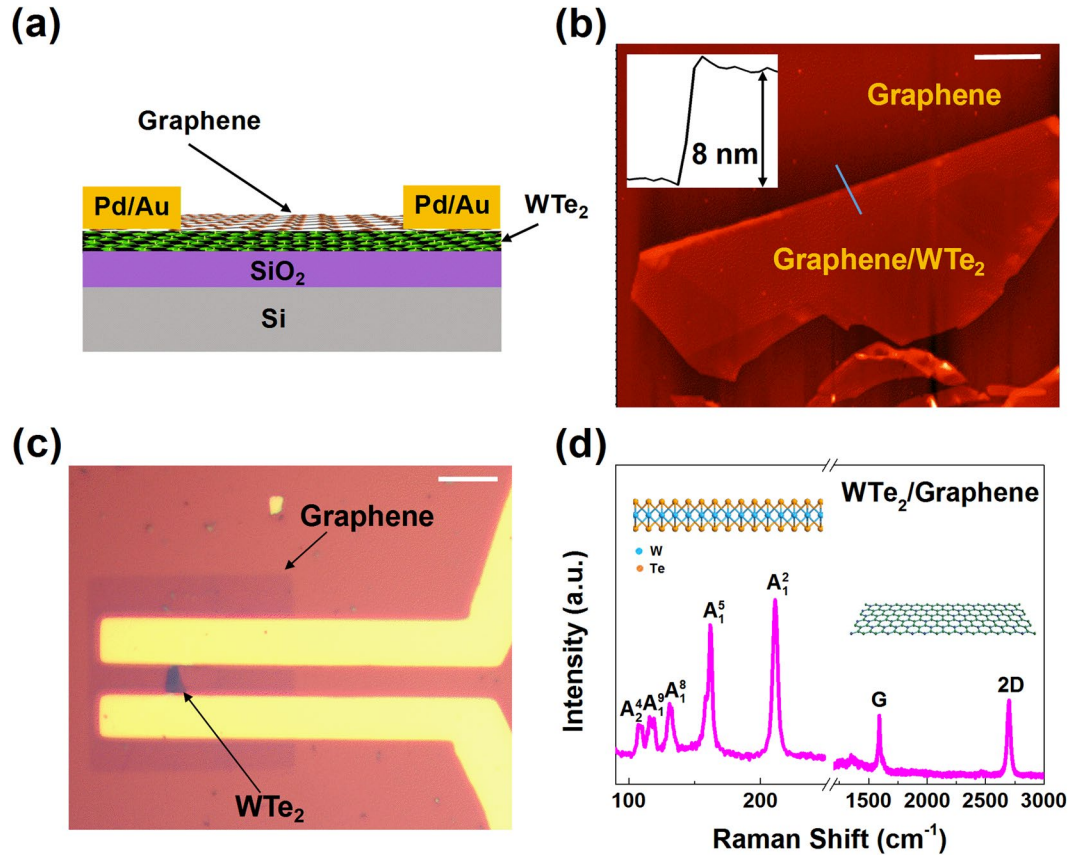

Figure 1. Graphene/WTe_2 heterostructure device. **(a)** Schematic illustration of the graphene/WTe_2 heterostructure-based device. **(b)** AFM image of the graphene/WTe_2 flakes. Inset shows cross-sectional height profile of the WTe_2 flake on the SiO_2/Si substrate. Scale: 2 μm. **(c)** Optical image of the fabricated graphene/WTe_2 hybrid device. Scale: 10 μm. The channel area of graphene/WTe_2 is 30 × 35 μm. **(d)** Raman spectrum for the graphene/WTe_2 heterostructure.

may yield new insights into the design and optimization of 2D materials based nanodevices. Here, we study the interfacial transport and photoresponse of all-semimetal graphene and WTe_2 heterostructure. Multi-fold of photocurrent enhancement, with a photoresponsivity ~8.7 A/W under 650 nm laser illumination, is observed in the graphene/WTe_2 hybrid device. Transport and photocurrent mapping suggest that both photovoltaic and photothermoelectric effects contribute to the enhancement of photocurrent. Our experimental results, provide new insights in the design of photonic functional vdWs heterostructures.

Results and Discussions

Figure 1a schematically illustrates the architecture of the device based on the graphene/WTe_2 heterostructure. Few-layer WTe_2 flakes were mechanically exfoliated onto the SiO_2/Si substrate. Chemical vapor deposition (CVD) grown monolayer graphene was then transferred onto the WTe_2 flakes using the polymethyl methacrylate (PMMA) supported procedures (see Methods for details). Optical contrast measurements were first used to identify the thickness of WTe_2 and graphene samples, and further characterizations were conducted by Raman spectroscopy, as shown in Supplementary Figure S1. The results indicate that both samples have good crystalline quality. It should be noted that the Raman features of the WTe_2 sample well coincide with its Td structure, confirming its semimetallic nature[38,44]. Figure 1b shows the AFM image of the graphene/WTe_2 stack. From the height profile of the WTe_2 flake on the substrate, the thickness of it is estimate to be ~8 nm, corresponding to ~10 layers of WTe_2. The heterostructure devices are prepared by a standard photolithography procedure (see Methods for details). Since thin WTe_2 flakes tend to degrade in ambient environment[45], a fatigue test of the graphene/WTe_2 film was conducted through optical contrast and Raman spectroscopy, in which the hybrid film showed no discernible change after 11 days of exposure in ambient conditions (see Supplementary Figure S2). The graphene layer is placed on top of WTe_2, which is envisioned to be effective in mitigating WTe_2 degradation or protecting inner layers of WTe_2 from further surface degradation affected by inevitable air exposure during device fabrication (that includes optical inspections to identify the hybrid film, spinning and backing the resist in photolithography to define the metal contacts and the channel, and the lift off process after the metal deposition). Figure 1c shows the optical micrograph of a representative graphene/WTe_2 device. The graphene channel is about 30 × 35 μm. The quality of the heterostructure device is confirmed by Raman spectroscopy again. As shown in Fig. 1d, the peak positions of both graphene and WTe_2 agree well with the previous results[38,46], confirming no significant perturbation to either material during the fabrication processes.

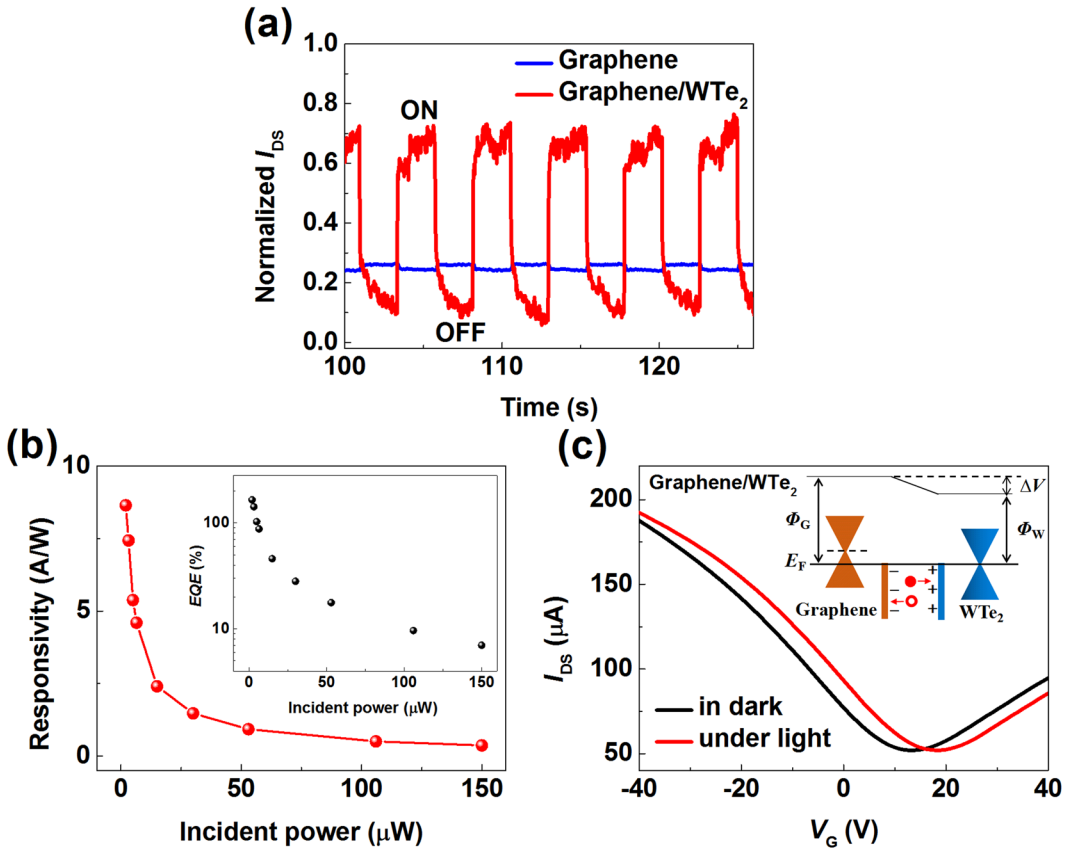

Figure 2. Photoresponse of the graphene/WTe_2 hybrid device. **(a)** Time-resolved photoresponse of the graphene/WTe_2 heterostructure device and pure graphene device under 650 nm laser switching on/off. **(b)** Responsivity of the graphene/WTe_2 phototransistor as function of the incident light power under 650 nm illumination. **(c)** *EQE* of the hybrid device as function of the incident light power under 650 nm illumination. **(d)** Transfer curves of the graphene/WTe_2 device in dark and under 650 nm laser illumination at $V_{DS} = 0.5$ V. Inset: Schematic diagram of potential step formation and the photo-induced carriers transporting process under light at the graphene-WTe_2 interface. Φ_G is the work function of graphene, Φ_W represents the work function of WTe_2, ΔV is the built-in potential difference. Solid sphere represents photo-induced electron, and hollow sphere is photo-induced hole.

To investigate the optoelectronic properties of the graphene and WTe_2 heterostructure and to provide insights into the hybridization of the all-semimetal interface, we conducted standard photocurrent measurements with a focused 650 nm continuous wave laser in vacuum ($<10^{-5}$ Torr) at room temperature. Figure 2a shows the normalized transient current response of the graphene/WTe_2 heterostructure and a pure graphene control sample with the same design (see Supplementary Figure S1). The transient current was recorded as the laser was turned on and off repeatedly at a fixed bias voltage of 0.5 V and the incident power is about 100 μW. As can be seen, the graphene/WTe_2 device maintains a long-term stability of its current in a series of periodic light stimulations. Moreover, the photocurrent of the heterostructure device demonstrates appreciable enhancement compared with that of the pure graphene device. Generally, Photoresponsivity (R) and external quantum efficiency (EQE) are the key figure-of-merit that are used to evaluate the performance of a photodetector. R is defined as the photocurrent at unit incident optical power and is given by:

$$R(\mathrm{A/W}) = I_{ph}/P_{opt}, \tag{1}$$

where I_{ph} is the photocurrent and P_{opt} is the incident light power on the effective area of the photodetectors. Apparently, high photoresponsivity indicates a large photocurrent can be achieved under relatively low incident illumination power. On the other hand, EQE characterizes the effectiveness of conversion of photons to electrons and is defined as:

$$EQE = hcI_{ph}/e\lambda P_{opt}, \tag{2}$$

where h is Planck's constant, c the velocity of light, e is the electronic charge and λ is the wavelength of the incident power. To compare with other devices, we measured the power-dependent photocurrent of the graphene/WTe_2 hybrid device at 650 nm (Supplementary Figure S3). The calculated values of R and EQE as functions of illumination power are plotted in Fig. 2b and its inset. As it can be seen, both R and EQE present non-linear

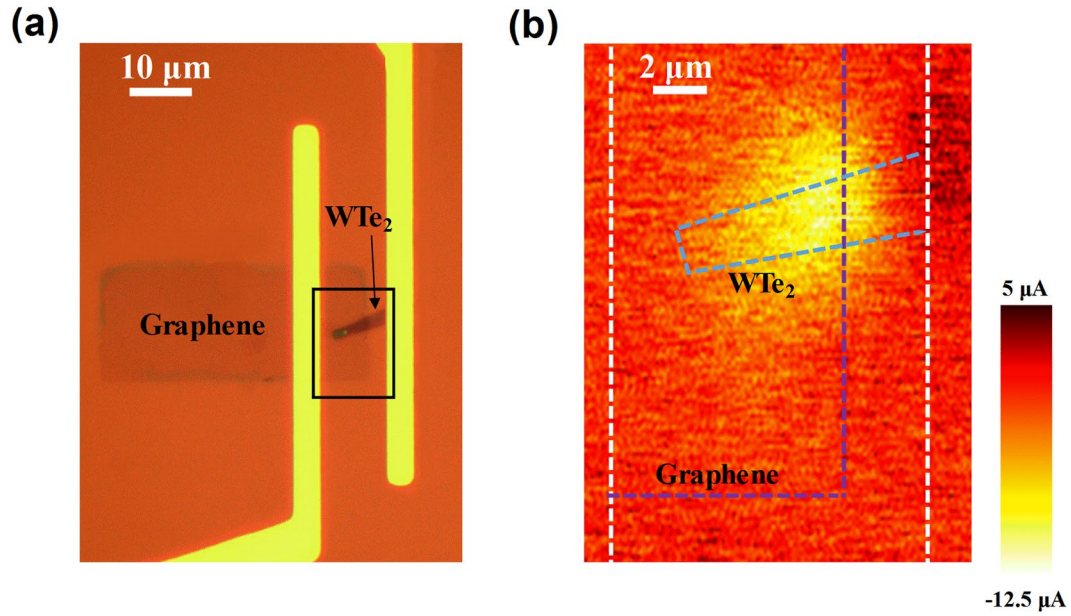

Figure 3. A staggered graphene/WTe_2 heterostructure device and photocurrent mapping. **(a)** An optical micrograph of the device, with graphene is staggered on top of WTe_2 flake. The area inside the black square is the scanned area. **(b)** Scanning photocurrent micrograph of the device acquired at $V_{DS} = 0.1$ V, with 0.6 μW power at 532 nm. Regions of photocurrent are observed in the overlapping area outlined by the WTe_2 flake (blue) with the patterned graphene film (purple). The electrodes are indicated by white dashed lines.

dependence on the incident light power, and their maximum values appear at low illumination power, which has also been observed in other graphene or MoS_2 based photodetectors[47–49]. For our specific case, the maximum value of *R* of the graphene/WTe_2 photodetector is ~8.7 A/W under 650 nm illumination, and the corresponding *EQE* is calculated to be 165% at a low incident power of 2 μW with $V_{DS} = 0.5$ V. These values are about two-three orders higher than the reported ones of pure monolayer graphene photodetectors[50–53], although they are lower than some of graphene-semiconductor heterostructures[54,55]. Our results for the first time demonstrate that an all-semimetal heterostructure can enable a pronounced photocurrent generation.

To shed lights on the photocurrent enhancement at the semimetal interface, it should be noted that due to the requirement of continuity of Fermi level, the difference in work function between metallic materials (i.e. a conventional 3D metal contact) and graphene can drive a charge transfer process, resulting in an inhomogeneous doping profiles (built-in field) along graphene, which is capable of separating light-induced electron-hole (e-h) pairs. To confirm such a 'photovoltaic' picture, transfer characteristics of the graphene/WTe_2 phototransistor in dark and under illumination were further studied as shown in Fig. 2c. It is seen that the charge neutrality point of the graphene/WTe_2 hybrid device, upon light irradiation, shifts to a larger positive voltage, unambiguously indicating a hole-doped effect of graphene (or photogenerated electrons transfer from graphene to WTe_2). Such a shift in transfer curve is compatible with the previously discussed Fermi level pinning effect, when considering the work function for graphene and WTe_2 are 4.5 eV and 4.39 eV, respectively[30,39]. It should be noted that the rather small work function mismatch (~0.1 eV) would lead to a built-in field that is weak and easily screened by impurity at the interface. The inset of Fig. 2c depicts the likely band bending scenario at the graphene/WTe_2 interface as stipulated by the difference in work function.

To further elaborate the photocurrent generation mechanism of the graphene/WTe_2 heterostructure, we fabricated a staggered graphene/WTe_2 heterostructure device as shown in Fig. 3a. The current-bias voltage (*I*-*V*) characteristic of the staggered graphene/WTe_2 device (Supplementary Figure S4) exhibits a slight deviation from the linear relationship, which provides evidence that a potential barrier exists at the graphene/WTe_2 junction. It should be noted that layer dependent transport measurement has recently suggested the likelihood of the opening of a small positive bandgap when the WTe_2 film is thinned below 9 nm. Such evolution of electronic structure of WTe_2 would also facilitate the establishment of a Schottky-like barrier at the graphene/WTe_2 interface[56]. Complex reconfiguration at the graphene and WTe_2 interface may also affected the potential barrier, which requires further more detailed investigation. Then we performed spatially resolved photocurrent measurement of the staggered graphene/WTe_2 heterostructure device under a green laser (532 nm, average power of 0.6 μW). As shown in Fig. 3b, the corresponding photocurrent mapping shows a pronounced photocurrent generation in the overlapping region of the graphene/WTe_2 junction, which further confirm the important role of the interfacial effects in the heterostructure system. Clearly, the photocurrent enhanced area in Fig. 3b does not exactly coincide with the heterostrcture region. As reported previously, the junction area of graphene due to Fermi level pinning can extend only 200–450 nm away from the metal contact into the graphene channel[32,33]. Therefore, photothermoelectric effect is considered to be another contributing factor to the photocurrent, which results from local heating of the graphene and WTe_2 junction due to the incident laser[57,58]. On one hand, inhomogeneous doping profiles

of the graphene and WTe_2 junction as mentioned above, give different Seebeck coefficients at the junction. On the other hand, considering graphene's excellent (up to 5000 $Wm^{-1}K^{-1}$) and WTe_2's rather poor (~3 $Wm^{-1}K^{-1}$) thermal conductivities[59,60], we assume that heat is accumulated in the graphene and WTe_2 junction when illuminated by light, which leads to a temperature gradient across the device. Then, a thermoelectric photocurrent was induced due to the different Seebeck coefficients and temperature gradient. Considering the small electron capacity and large light-induced changes in electron temperature in graphene, the photothermoelectric effect may play as important a role as in the photovoltaic effect. Investigation of photocurrent generation as a function of layer thickness therefore would yield more insights into the interfacial charge transfer dynamics but is beyond the scope of the current study.

In conclusion, we demonstrated an all-semimetal vdWs heterostructure device through the integration of few-layer WTe_2 flakes with monolayer graphene. The photocurrent investigation suggests that, despite the all-semimetal nature of the heterostructure (by graphene and few-layer WTe_2), the interfacial effects can effectively separate the photo-induced electron-hole pairs and lead to pronounced photocurrent enhancement, both due to photovoltaic and photothermoelectric effects. A photoresponsivity ~8.7 A/W is obtained for the heterostructure device under 650 nm laser illumination. These results advance the understanding of fundamental properties of all-semimetal heterostructures and provide guidelines for designing novel photonic devices.

Methods

Mechanical exfoliation of WTe_2. A standard mechanical exfoliation method was employed to isolate few-layer WTe_2 flakes and transferred them onto a highly doped Si wafer capped by a 285-nm-thick SiO_2 layer. Thickness of the exfoliated WTe_2 flakes was measured by means of optical contrast and Raman spectra.

Transfer of grapheme. A 0.5 cm × 0.5 cm CVD grown monolayer graphene coated with PMMA on copper was immersed in ammonium persulfate for 3 h and deionized water for 30 min, respectively. Subsequently, the graphene film supported by PMMA was transferred onto the WTe_2 flakes. The PMMA was immediately removed using hot acetone (60 °C).

Fabrication of devices. The source and drain electrodes (Pd/Au, 10 nm/40 nm) were deposited on top of the graphene/WTe_2 stacks through a shadow mask by electron beam evaporation. The graphene/WTe_2 channel was patterned using photolithography procedure and oxygen plasma etching.

Raman spectroscopy and AFM measurements. The Raman spectroscopy measurements were carried out using a Horiba Jobin Yvon LabRAM HR-800 Raman spectrometer with a 514 nm argon ion laser. Surface morphology of the films was studied using atomic force microscopy (AFM) (Cypher, Asylum Research Inc.).

Photoresponse characterization. For photoresponse characterization, the 650 nm laser beam is guided through an optical fiber with a FC/PC ferrule and is subsequently incident onto the channel of the devices without focusing. The beam at the device was measured to be Gaussian-shaped with a diameter of about 300 μm. The electrical measurements were conducted using a semiconductor parameter analyzer (Keithley 4200) in a closed cycle cryogenic probe station under vacuum ($<10^{-5}$ Torr) at room-temperature. The photocurrent mapping was performed in a custom data collecting system with a 532 nm continuous wave laser generator, a mechanical chopper, a source meter (Keithley 2612B), and a lock-in amplifier (SR830, Stanford Research Systems Inc.). The transport characterization of the staggered device was measured under vacuum at 24 K for suppressing the outside interference.

References

1. Geim, A. K. & Grigorieva, I. V. Van derWaals heterostructures. *Nature* **499**, 419–425 (2013).
2. Liu, Y. *et al*. Van der Waals heterostructures and devices. *Nature Reviews Materials*, 16042 (2016).
3. Choi, K., Lee, Y. T. & Im, S. Two-dimensional van der Waals nanosheet devices for future electronics and photonics. *Nano Today* **11**, 626–643 (2016).
4. Novoselov, K. S., Mishchenko, A., Carvalho, A. & Castro Neto, A. H. 2D materials and van der Waals heterostructures. *Science* **353**, 6298 (2016).
5. Duesberg, G. S. Heterojunctions in 2D semiconductors: A perfect match. *Nat. Mater.* **13**, 1075–1076 (2014).
6. Haigh, S. J. *et al*. Cross-sectional imaging of individual layers and buried interfaces of graphene-based heterostructures and superlattices. *Nat. Mater.* **11**, 764–767 (2012).
7. Novoselov, K. S. *et al*. Two-dimensional gas of massless Dirac fermions in graphene. *Nature* **438**, 197–200 (2005).
8. Song, L. *et al*. Large scale growth and characterization of atomic hexagonal boron nitride layers. *Nano Lett.* **10**, 3209–3215 (2010).
9. Mak, K. F., Lee, C., Hone, J., Shan, J. & Heinz, T. F. Atomically thin MoS_2: A new direct-gap semiconductor. *Phys. Rev. Lett.* **105**, 136805 (2010).
10. Mak, K. F. & Shan, J. Photonics and optoelectronics of 2D semiconductor transition metal dichalcogenides. *Nat. Photonics* **10**, 216–226 (2016).
11. Zhang, W., Wang, Q., Chen, Y., Wang, Z. & Wee, A. T. S. Van der Waals stacked 2D layered materials for optoelectronics. *2D Materials* **3**, 022001 (2016).
12. Roy, K. *et al*. Graphene-MoS_2 hybrid structures for multifunctional photoresponsive memory devices. *Nat. Nanotechnol.* **8**, 826–830 (2013).
13. Lee, C.-H. *et al*. Atomically thin p-n junctions with van der Waals heterointerfaces. *Nat. Nanotechnol.* **9**, 676–681 (2014).
14. Doan, M.-H. *et al*. Charge transport in MoS_2/WSe_2 van der Waals heterostructure with tunable inversion layer. *ACS Nano* **11**, 3832–3840 (2017).
15. Zhu, C. *et al*. A robust and tunable mid-infrared optical switch enabled by bulk Dirac fermions. *Nat. Commun.* **8**, 14111 (2017).
16. Zhu, C. *et al*. Broadband hot-carrier dynamics in three-dimensional Dirac semimetal Cd_3As_2. *Appl. Phys. Lett.* **111**, 091101 (2017).
17. Wang, Q. *et al*. Ultrafast broadband photodetectors based on three-dimensional Dirac semimetal Cd_3As_2. *Nano Lett.* **17**, 834–841 (2017).
18. Meng, Y. *et al*. Three-dimensional Dirac semimetal thin-film absorber for broadband pulse generation in the near-infrared. *Opt. Lett.* **43**, 1503 (2018).

19. Gao, M. *et al*. Tuning the transport behavior of centimeter-scale WTe_2 ultrathin films fabricated by pulsed laser deposition. *Appl. Phys. Lett.* **111**, 031906 (2017).
20. Soluyanov, A. A. *et al*. Type-II Weyl semimetals. *Nature* **527**, 495–498 (2015).
21. Zhou, J. *et al*. Large-area and high-quality 2D transition metal telluride. *Adv. Mater.* **29**, 1603471 (2017).
22. Britnell, L. *et al*. Strong light-matter interactions in heterostructures of atomically thin films. *Science* **340**, 1311–1314 (2013).
23. Massicotte, M. *et al*. Picosecond photoresponse in van der Waals heterostructures. *Nat. Nanotechnol.* **11**, 42–46 (2016).
24. Tian, H. *et al*. Novel field-effect Schottky barrier transistors based on graphene-MoS_2 heterojunctions. *Sci. Rep.* **4**, 5951 (2014).
25. Shanmugam, M., Jacobs-G., R., Song, E. S. & Yu, B. Two-dimensional layered semiconductor/graphene heterostructures for solar photovoltaic applications. *Nanoscale* **6**, 12682–12689 (2014).
26. Wu, Y., Yang, W., Wang, T., Deng, X. & Liu, J. Broadband perfect light trapping in the thinnest monolayer graphene-MoS_2 photovoltaic cell: The new application of spectrum-splitting structure. *Sci. Rep.* **6**, 20955 (2016).
27. Britnell, L. *et al*. Resonant tunnelling and negative differential conductance in graphene transistors. *Nat. Commun.* **4**, 1794 (2013).
28. Britnell, L. *et al*. Field-effect tunneling transistor based on vertical graphene heterostructures. *Science* **335**, 947–950 (2012).
29. Withers, F. *et al*. Light-emitting diodes by band-structure engineering in van der Waals heterostructures. *Nat. Mater.* **14**, 301–306 (2015).
30. Xia, F., Perebeinos, V., Lin, Y., Wu, Y. & Avouris, P. The origins and limits of metal graphene junction resistance. *Nat. Nanotechnol.* **6**, 179–184 (2011).
31. Giovannetti, G. *et al*. Doping graphene with metal contacts. *Phys. Rev. Lett.* **101**, 026803 (2008).
32. Mueller, T., Xia, F., Freitag, M., Tsang, J. & Avouris, P. Role of contacts in graphene transistors: A scanning photocurrent study. *Phys. Rev. B* **79**, 245430 (2009).
33. Xia, F. *et al*. Photocurrent imaging and efficient photon detection in a graphene transistor. *Nano Lett.* **9**, 1039–1044 (2009).
34. Xu, Y. *et al*. Contacts between two- and three- dimensional materials: Ohmic, Schottky, and p-n heterojunctions. *ACS Nano* **10**, 4895–4919 (2016).
35. Xie, C., Mak, C., Tao, X. & Yan, F. Photodetectors based on two-dimensional layered materials beyond graphene. *Adv. Funct. Mater.* **27**, 1603886 (2016).
36. Wang, J. *et al*. Recent progress on localized field enhanced two-dimensional material photodetectors from ultraviolet-visible to infrared. *Small* **13**, 1700894 (2017).
37. Xia, W. *et al*. Recent progress in van der Waals heterojunctions. *Nanoscale* **9**, 4324–4365 (2017).
38. Lee, C. H. *et al*. Tungsten Ditelluride: A layered semimetal. *Sci. Rep.* **5**, 10013 (2015).
39. Torun, E., Sahin, H., Cahangirov, S., Rubio, A. & Peeters, F. M. Anisotropic electronic, mechanical, and optical properties of monolayer WTe_2. *Journal of Applied Physics* **119**, 074307 (2016).
40. Song, Q. *et al*. The in-plane anisotropy of WTe_2 investigated by angle-dependent and polarized Raman spectroscopy. *Sci. Rep.* **6**, 29254 (2016).
41. Dai, Y. M. *et al*. Ultrafast carrier dynamics in the large-magnetoresistance material WTe_2. *Phys. Rev. B* **92**, 161104 (2015).
42. Koo, J. *et al*. Near-infrared saturable absorption of defective bulk-structured WTe_2 for femtosecond laser mode-locking. *Adv. Funct. Mater.* **26**, 7454 (2016).
43. Liu, Y., Stradins, P. & Wei, S. Van der Waals metal-semiconductor junction: Weak Fermi level pinning enables effective tuning of Schottky barrier. *Sci. Adv.* **2**, e1600069 (2016).
44. Jiang, Y., Gao, J. & Wang, L. Raman fingerprint for semimetal WTe_2 evolving from bulk to monolayer. *Sci. Rep.* **6**, 19624 (2016).
45. Ye, F. *et al*. Environmental instability and degradation of single- and few-layer WTe_2 nanosheets in ambient conditions. *Small* **12**, 5802–5808 (2016).
46. Li, X. *et al*. Transfer of large-area graphene films for high-performance transparent conductive electrodes. *Nano Lett.* **9**, 4359–4363 (2009).
47. Liu, Y. *et al*. Planar carbon nanotube-graphene hybrid films for high-performance broadband photodetectors. *Nat. Commun.* **6**, 8589 (2015).
48. Sun, M. *et al*. Novel transfer behaviors in 2D MoS_2/WSe_2 heterotransistor and its applications in visible-near infrared photodetection. *Adv. Electron. Mater.* **3**, 1600502 (2017).
49. Feng, W. *et al*. Ultrahigh photo-responsivity and detectivity in multilayer InSe nanosheets phototransistors with broadband response. *J. Phys. Chem. C* **3**, 7022 (2015).
50. Xia, F., Mueller, T., Lin, Y., Valdes-G., A. & Avouris, P. Ultrafast graphene photodetector. *Nat. Nanotechnol.* **4**, 839–843 (2009).
51. Mueller, T., Xia, F. & Avouris, P. Graphene photodetectors for high-speed optical communications. *Nat. Photonics* **4**, 297–301 (2010).
52. Liu, Y. *et al*. Plasmon resonance enhanced multicolour photodetection by graphene. *Nat. Commun.* **2**, 579 (2011).
53. Echtermeyer, T. *et al*. Strong plasmonic enhancement of photovoltage in graphene. *Nat. Commun.* **2**, 458 (2011).
54. Yu, W. *et al*. Near-infrared photodetectors based on $MoTe_2$/graphene heterostructure with high responsivity and flexibility. *Small*, 1700268 (2017).
55. Gao, A. *et al*. Gate-tunable rectification inversion and photovoltaic detection in graphene/WSe_2 heterostructures. *Appl. Phys. Lett.* **108**, 223501 (2016).
56. Zheng, F. *et al*. On the quantum spin hall gap of monolayer 1T'-WTe_2. *Adv. Mater.* **28**, 4845–4851 (2016).
57. Echtermeyer, T. J. *et al*. Photothermoelectric and photoelectric contributions to light detection in metal-graphene-metal photodetectors. *Nano Lett.* **14**, 3733–3742 (2014).
58. Sun, Z. & Chang, H. Graphene and graphene-like two-dimensional materials in photodetection: mechanisms and methodology. *ACS Nano* **8**, 4133–4156 (2014).
59. Balandin, A. A. *et al*. Superior Thermal Conductivity of Single-Layer Graphene. *Nano Lett.* **8**, 902–907 (2008).
60. Mleczko., M. J. *et al*. High current density and low thermal conductivity of atomically thin semimetallic WTe_2. *ACS Nano* **10**, 7504–7514 (2016).

Acknowledgements

This work was supported in part by the State Key Project of Research and Development of China (2017YFA0206304); the National Basic Research Program of China (2014CB921101, 2011CB301900); National Natural Science Foundation of China (61775093, 61427812); National Young 1000 Talent Plan; A 'Jiangsu Shuangchuang Team' Program; Jiangsu NSF (BK20170012, BK20140054); and Australian Research Council (DP 160101474).

Author Contributions

F.W. conceived the project and together with R.Z. supervised the project. Y.L. performed the major part of the experiments. C.L. and X.W. contributed to the measurement of photocurrent mapping. The transport results and data analysis were discussed between F.W., L.H. and X.W. F.W., Y.B.X. and Y.S. co-wrote the paper. All authors contributed to the discussion and preparation of the manuscript and gave their approval to the final version.

Additional Information

Supplementary information accompanies this paper at https://doi.org/10.1038/s41598-018-29717-8.

Competing Interests: The authors declare no competing interests.

Publisher's note: Springer Nature remains neutral with regard to jurisdictional claims in published maps and institutional affiliations.